Multidimensional imbalances in cortical circuit activity in Fragile-X Syndrome mice

Cian O'Donnell[1,2,*], J. Tiago Gonçalves[3,4], Carlos Portera-Cailliau[3] and Terrence J. Sejnowski[2,5,*]

[1]Department of Computer Science, University of Bristol, Bristol, UK
[2]Howard Hughes Medical Institute, Salk Institute for Biological Studies, La Jolla CA, USA
[3]Departments of Neurology and Neurobiology, David Geffen School of Medicine at UCLA, Los Angeles, CA, USA
[4]Dominick Purpura Department of Neuroscience, Albert Einstein College of Medicine, Bronx, NY, USA
[5]Division of Biological Sciences, University of California at San Diego, La Jolla, CA, USA
*Correspondence: cian.odonnell@bristol.ac.uk (C.O'D.), terry@salk.edu (T.J.S.)

Abstract

A leading theory for multiple brain disorders, such as schizophrenia and autism, is that they arise from developmental imbalances in excitatory and inhibitory (E/I) brain circuitry. However, it is unclear whether this simple 1-dimensional model is sufficiently rich to capture the set of key alterations of neural circuit processing in brain disorders. Here we used a combination of computational modeling and large-scale analysis of *in vivo* 2-photon Ca^{2+} imaging data from somatosensory cortex of wild-type and *Fmr1* knock-out (KO) mice, a model of Fragile X syndrome, to test the E/I imbalance model. Our main findings were: 1) the E/I imbalance model was not rich enough to capture the alterations in neural activity statistics in *Fmr1* KO mice; 2) in a computational model we found greatly varying magnitudes and directions of effects of synaptic and cellular properties on network activity; 3) evidence for opposite changes in circuit properties of *Fmr1* KO mice at different stages of development; 4) a reduction in the entropy of circuit activity in young *Fmr1* KO mice compared to wild-type, but an opposite increase in adult *Fmr1* KO mice. These findings suggest qualitatively new strategies for developing treatments for Fragile-X Syndrome and related disorders.

Introduction

The nervous system shows complex organization at many spatial scales: from genes and molecules, to cells and synapses, to neural circuits. Ultimately, the electrical and chemical signaling at all of these levels must give rise to the behavioral and cognitive processes seen at the whole-organism level. When trying to understand prevalent brain disorders such as Autism and Schizophrenia, a natural question to ask is: where does the most productive level of neuroscientific investigation lie? Traditionally, most major disorders are diagnosed entirely at the behavioral level, whereas pharmaceutical interventions are targeted at correcting alterations at the molecular level. Even for the most successful drugs, we have little understanding of how these pharmaceutical actions at the molecular level percolate up the organizational ladder to affect behavior and cognition. This implies that a promising level of analysis might be at the intermediate level of neural circuits, for two reasons. First, circuits are closer to the behavioral level than the molecular signaling of cells is; therefore, it might be easier to predict how interventions at the circuit level affect behavior. Second, since we have fewer neurons than molecules and fewer neural circuits than neurons, the dimensionality of the brain's neural circuit properties is likely much smaller than that of the brain's molecular properties. It might turn out to be easier to find interventions to push circuit-level properties of brain disorder patients towards the operating regimes observed in healthy subjects, than it would be to correct the corresponding deficits in patients at the molecular level.

One prominent circuit-level hypothesis for brain disorders has been the idea of an imbalance in excitatory and inhibitory signaling. First proposed as a model for Autism (Rubenstein and Merzenich, 2003), the concept has since been applied to many other brain disorders, including Schizophrenia, Rett Syndrome, Fragile-X Syndrome, Tuberous Sclerosis, and Angelman Syndrome (Bateup et al., 2011; Dani et al., 2005; Gibson et al., 2008; Kehrer et al., 2008; Wallace et al., 2012). However, a major drawback of this model in its simplest form is that it is entirely 1-dimensional. It implies that either too much excitation or too much inhibition is unhealthy, and by extension that the symptoms of these disorders could be normalized by either enhancing or reducing the level of, say, GABAergic signaling as appropriate. Although

clinical trials for such GABAergic-based interventions are ongoing (Braat and Kooy, 2015), no treatment for a neurodevelopmental disorder based on this principle has yet been validated.

In this study we compare *in vivo* neocortical circuit activity data recorded from wild-type and Fragile-X model mice, and find that the classic 1-dimensional E/I imbalance model is not flexible enough to capture the observed differences. Instead, we argue that higher-dimensional models are needed. We demonstrate that a novel 2D neural circuit model can account for many of the differences in circuit activity that are likely important for neural coding and information processing. Finally, we apply a recently developed large-scale data analysis method to our Ca^{2+} imaging data to uncover systematic shifts in neural circuit entropy across development in Fragile-X.

Results

Neural circuits consist of many components, connected together in a complicated fashion. These components typically interact non-linearly to generate circuit activity dynamics. Although many properties of cortical circuit components have been found to be altered in animal models of brain disorders, it remains extremely difficult to predict the net effect of varying any one particular parameter on circuit behavior.

To explore this issue more concretely, we built a computational model of layer (L) 2/3 mouse somatosensory cortex. This circuit has been studied in detail by neurophysiologists, and several of its properties have been found to be altered during development in mouse models of Fragile-X syndrome, including parvalbumin-positive interneuron number (Selby et al., 2007), GABA receptor reversal potential (He et al., 2014), dendritic spine dynamics (Cruz-Martin et al., 2010), and L4 excitatory input (Bureau et al., 2008), reviewed by (Contractor et al., 2015). In the ideal case we would like to derive a mathematical relationship between any arbitrary circuit parameter and its effect on circuit function, but for even reasonably complicated models this problem quickly becomes analytically intractable. Because of this difficulty, we used numerical computer simulations to perform hypothetical experiments where we perturbed various parameters of the circuit model and observed the resulting changes in circuit-level activity dynamics.

The L2/3 computational model we built (Figure 1A, see Methods for details) consisted of four interconnected populations of leaky integrate-and-fire neurons: one group of 1700 excitatory (E) pyramidal neurons and three groups of inhibitory neurons: 115 $5HT_{3A}R$-expressing neurons, 70 parvalbumin-expressing (PV) neurons, and 45 somatostatin-expressing (SOM) neurons. This L2/3 circuit was driven by a separate population of 1500 L4 excitatory neurons. Cellular numbers, intrinsic properties, synaptic strengths, and connectivity statistics were taken from published *in vitro* data from P17—22 wild-type mice (Avermann et al., 2012; Lefort et al., 2009; Tomm et al., 2014).

L2/3 neurons of the rodent somatosensory neocortex respond only sparsely to sensory stimulation *in vivo*. For example, twitching a whisker activates only ~20% of neurons on

average, each of which typically emits only one action potential (Clancy et al., 2015; Kerr et al., 2007; Sato et al., 2007). Hence any individual neuron carries very little information about the stimulus on its own, implying that information must instead be encoded at the circuit level as the identities of the subset of neurons that respond.

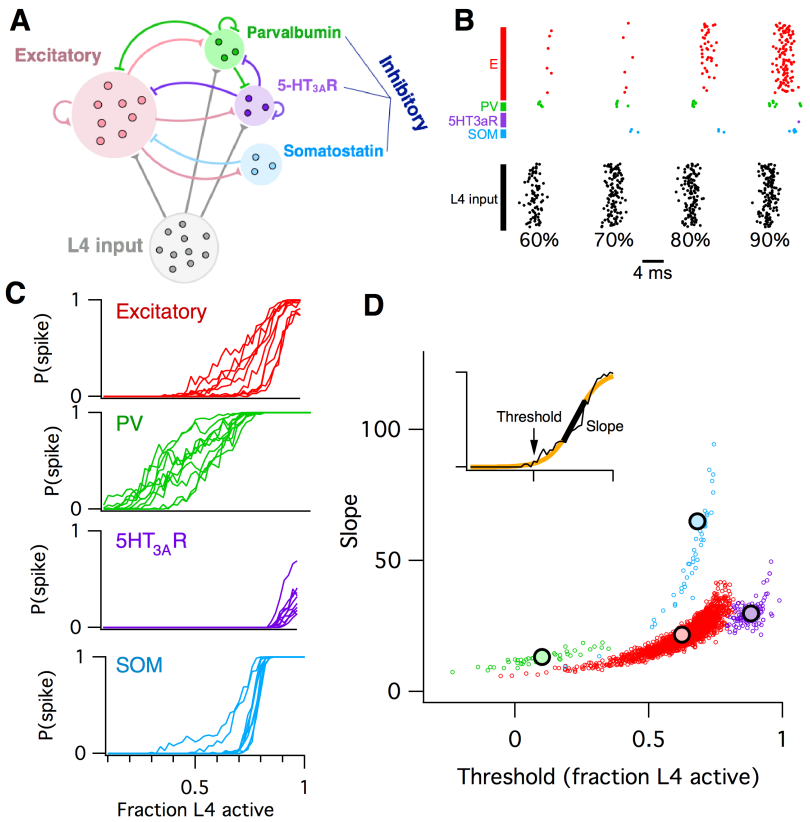

Figure 1. Computational model of L2/3 mouse somatosensory cortex.
A: Schematic diagram of computational circuit model.
B: Example raster plots of spiking responses from a subset of neurons from each cell type (colors as in panel A), for varying fractions of L4 activated (black).
C: Probability of spiking as a function of the fraction of L4 neurons activated. Each curve represents the response probability of a single neuron, averaged over multiple trials and multiple permutations of active L4 cells.
D: Each circle plots the fitted logistic slope and threshold values for a single neuron in the simulation. Circle color indicates cell type: red is excitatory, green is PV inhibitory, purple is 5ht3AR inhibitory, blue is SOM inhibitory. Inset shows an example fitted logistic response function (orange) to the noisy simulation results from a single excitatory neuron (black).

To model whisker twitching, we simulated a volley of spikes arriving from L4 as input to the population of L2/3 cells. We chose a random subset of L4 neurons as ON, then sent a single spike from each of these L4 cells to their target neurons in L2/3, and recorded the responses of

all neurons in L2/3, some of which spiked and some of which did not. We repeated this identical stimulation multiple times, in order to get an average response probability for each L2/3 neuron, given the probabilistic vesicle release at synapses in the model. Then we chose a different random subset of L4 neurons as ON, and repeated the entire procedure. Finally, we varied the fraction of L4 cells active and plotted the probability of response for each individual L2/3 neuron as a function of L4 activity level (Figure 1B—C).

We found that the mean response probability of each neuron in the simulation increased from zero to one monotonically with increasing L4 activity level. However, the shape of the response curve varied systematically across cell types, and was heterogeneous for different neurons of a given cell type. To quantify these differences, we used logistic regression to fit the response profile of each neuron with a sigmoid function (Figure 1D, inset), which has just two parameters: the slope (representing the steepness of the response curve) and threshold (representing the minimal fraction of L4 neurons needed to activate the cell). When we plotted the fitted slope and threshold values for each neuron against each other, we found that each cell type falls into a distinct cluster in this 2-dimensional space. For example, all PV inhibitory neurons had a low slope and low threshold, whereas SOM inhibitory neurons had a steep slope and moderate threshold. We will use these slope-threshold measurements to summarize the circuit-level input-output function of this 'default' model of L2/3 somatosensory cortex.

The circuit model contains 100 parameters (Methods), several of which are altered in Fragile-X mouse models. How sensitive is the circuit's macroscopic input-output function to alterations in its low-level components? To test this, we varied 76 of the model parameters in turn by ±20%, and repeated the entire set of simulations for each case (Methods). For each individual parameter alteration, we fit a new logistic response function for each model neuron. We summarize the results by plotting the logistic slope and threshold parameters and comparing their values to those found with the default model. The outcomes were hugely varied. We show three examples from the set of fifty-nine in Figure 2A. First, when we increased the amplitude of postsynaptic potentials (PSPs) of excitatory synapses from L4 to L2/3 excitatory neurons, we found that the logistic threshold parameter of all cell types shifted leftwards to lower values (Figure 2A left), implying that fewer L4 neurons were needed to activate the entire L2/3 circuit.

In contrast, when we increased the PSP amplitude of a different excitatory synapse, the recurrent connections between L2/3 excitatory neurons, we found (Figure 2A center) that excitatory and SOM inhibitory neurons had increased slope parameters relative to default, with little change in their threshold parameters. $5HT_{3A}R$

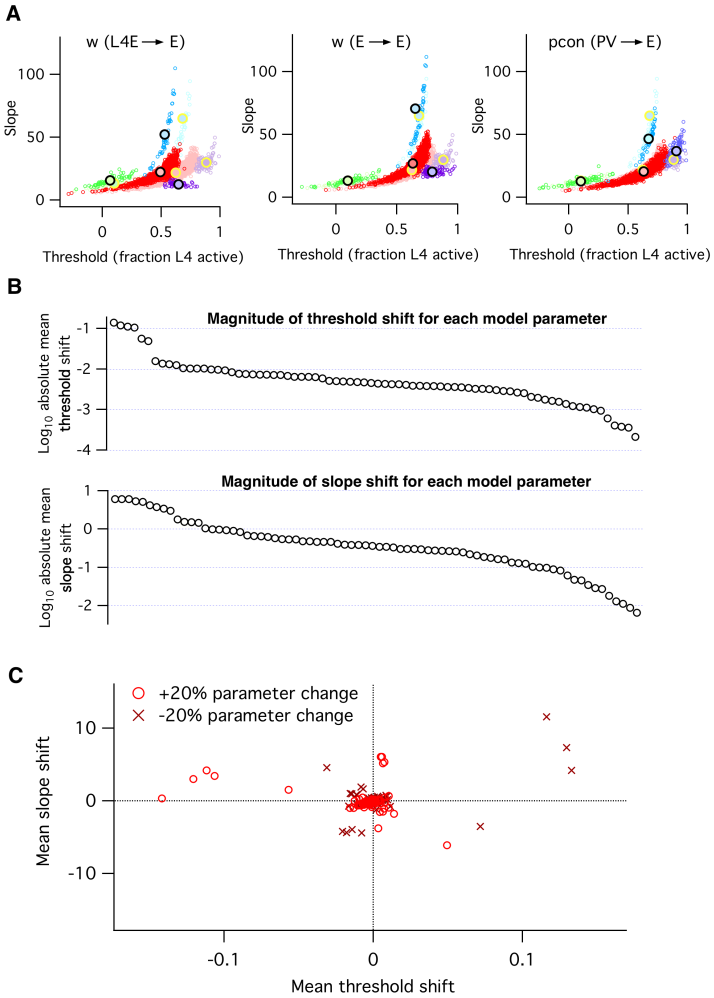

Figure 2. Heterogeneous effects of varying L2/3 parameters on the circuit input-output function.

A: Shifts in the distribution of fitted slope and threshold parameters as a result of increasing the strength of synapses from L4 to L2/3 E neurons (left), increasing the strength of recurrent synapses between L2/3 E neurons (center), or increasing the connection probability between L2/3 PV interneurons and E neurons (right). Transparent circles represent values for default network, heavy circles for altered network. The default and altered group means are large yellow and black open circles, respectively.

B: Absolute values of mean shifts in threshold (upper plot) and slope (lower plot) for E neurons arising from increasing the value of each parameter by +20%. Note that data are presented on a log10 scale.

C: The shift in mean slope-threshold parameter values for E neurons from the default

network values, in response to each of the 59 circuit parameter alterations. Light red circles indicate +20% increase in parameter value; dark red crosses indicate a -20% decrease in parameter value.

134 inhibitory neurons had decreased slopes and thresholds, while PV neurons had little change at
135 all. As a third example we increased the probability of inhibitory synaptic connections from L2/3
136 PV interneurons to L2/3 excitatory neurons (Figure 2A right). In this case we found that
137 excitatory neurons had a lower slope and increased threshold, SOM inhibitory neurons had a
138 lower slope, $5HT_{3A}R$ inhibitory neurons had both an increased slope and threshold, and PV
139 neurons showed little change, even though their outgoing synapses were the parameter that
140 was altered.

141 To synthesize the findings from all simulations, for each altered parameter we plot the shift in
142 mean slope-threshold values for L2/3 excitatory neurons from the mean values found with the
143 default model (Figure 2B). We focus on excitatory neurons because they constitute 90% of the
144 neurons in this layer (Lefort et al., 2009) and are the primary output to downstream circuits
145 (Mao et al., 2011; Petreanu et al., 2007). Overall, we found a very heterogeneous picture. First,
146 the magnitude of the shift in circuit response varied dramatically from parameter to parameter
147 (Figure 2B—C). Varying some parameters, such as the first two examples given above, had
148 large effects, whereas varying other parameters such as w_{I5htE} (the strength of synapses from
149 $5HT_{3A}R$ inhibitory neurons to E neurons) or τm_{Isom} (the membrane time constant of SOM
150 inhibitory neurons) had little effect. Second, the direction of shift in 2-D slope-threshold space
151 also depended on parameter (Figure 2C). Increasing some parameters changed either circuit
152 slope or threshold in isolation, while other parameters changed both slope and threshold
153 together. All four quadrants of the slope-threshold plane could be reached by various subsets
154 of the model parameters. Third, basic knowledge of whether a component was 'excitatory' or
155 'inhibitory' was insufficient to predict the direction of slope-threshold change. For example, the
156 two glutamatergic projections considered in Figure 2A had distinct effects on circuit function.

157 In summary, these simulations indicate that the L2/3 somatosensory cortex circuit has
158 extremely varied sensitivities to changes in its cellular components, and that the eventual
159 circuit-level consequences cannot be predicted from knowledge of the class of the perturbed
160 neurotransmitter alone.

161 ***Firing rates and correlations from the logistic model***

162 Above we investigated how low-level circuit components affect a high-level circuit input-output
163 function, as parameterized by the slope and threshold of fitted logistic functions. But how is this
164 logistic input-output function related to more common measures of neural population activity,
165 such as firing rates and pairwise correlations between neurons? To investigate this, we
166 considered the following reduced statistical model of cortical activity. We assumed for
167 simplicity that the magnitude of the total input to the L2/3 circuit is a Gaussian distributed
168 random variable, with zero mean and unit standard deviation (Figure 3A lower left). Then we
169 described each L2/3 neuron's input-output as a logistic function as before (Figure 3A upper
170 left), with threshold and slope defined relative to the Gaussian input's mean and standard
171 deviation, respectively. Given this model, we can numerically calculate the probability
172 distribution over a neuron's firing probability, which in general is skewed and non-Gaussian
173 (Figure 3A upper right). From this function we compute (Methods) both the neuron's mean
174 firing probability and the pairwise correlation of two identical neurons following this profile
175 (Figure 3A lower right).

176 Neural firing rates and correlations had qualitatively different dependencies on the underlying
177 logistic model's slope and threshold. Neural firing rate was greatest when threshold was low
178 and slope was high (top left of phase plot, Figure 3C left), whereas correlations were greatest
179 when both threshold and slope were high (top right of phase plot, Figure 3C right). This implies
180 that any change in the circuit's input-output function slope or threshold will in general have
181 distinct effects on firing rate versus correlations, and so could not be captured by a 1-
182 dimensional E/I balance model that sought to normalize firing rates alone. To illustrate this fact,
183 we plot the calculated correlation values along a contour where firing probability is fixed at 0.1
184 (Figure 3D). In the region of parameter space where both the slope and threshold are low
185 (Figure 3C bottom left), correlations are low, ~0.01. However, as we move along the contour
186 for firing rate = 0.1 towards the region of parameter space where slope and threshold are high
187 (Figure 3C top right), the pairwise correlations increase to ~0.4. This shows that a 1-
188 dimensional E/I balance rule that exclusively sought to normalize neural firing rates would
189 leave neural correlations free to achieve arbitrary values.

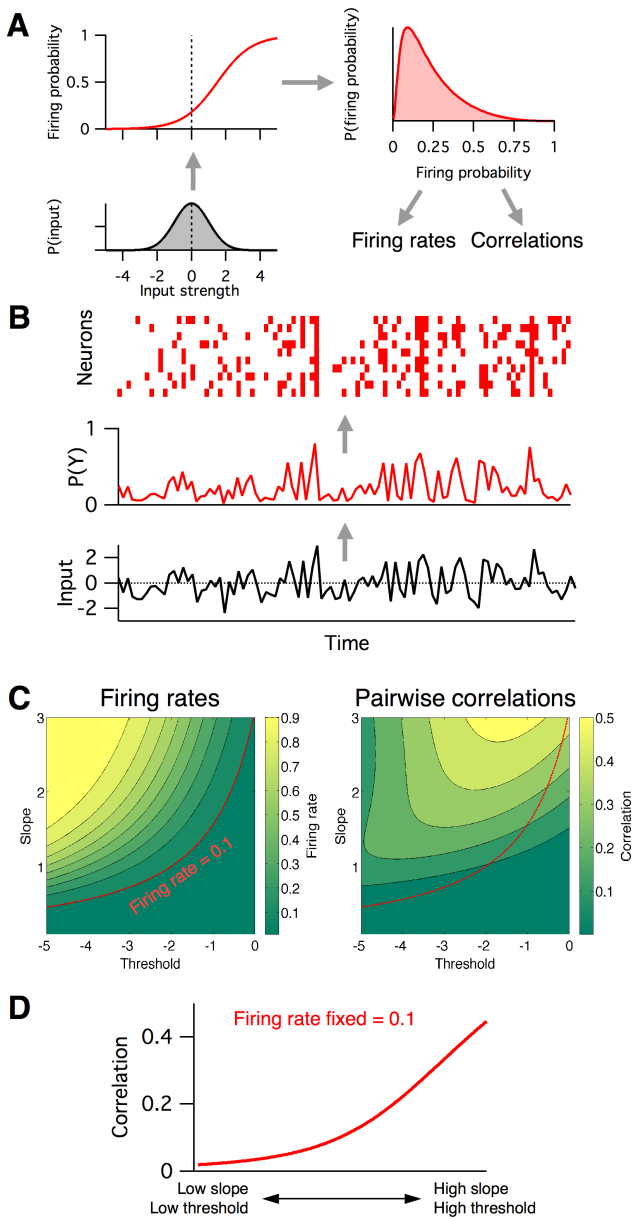

Figure 3. Firing rates and pairwise correlations from the logistic response model.
A: Logistic model components. We assume a normally distributed input drive (gray distribution, bottom left), which is passed through the neuron's probabilistic spike input-output function (red curve, top left), which results in a distribution of spike probabilities (top right) that are determined by the input-output function's slope and threshold parameters. From the output distribution we can directly calculate the mean firing rate and correlation between a pair of such neurons (Methods).
B: Example spikes from the logistic model. The bottom trace (black) shows examples inputs over time drawn randomly from the same normal distribution. This is transformed to spike probability at each time point (red trace). Example spike trains can then be generated from the spike probability trace by drawing Bernoulli samples with the specified probabilities (red ticks, top). If each neuron's spike train is conditionally independent given the same spike

probabilities, we can see correlations in their spike trains.
C: Calculated mean firing rate (left) and pairwise correlation (right) color maps as a function of the logistic threshold (x-axis) and slope (y-axis) parameters. Contours indicate lines of fixed firing rate or correlation in the 2D slope-threshold space.
D: Pairwise correlation values along the slope-threshold contour for firing rate = 0.1.

How might these findings inform our understanding of neurodevelopmental disorders, such as Fragile-X syndrome? To explore this we fit the parameters of the logistic model to reproduce the statistics of spontaneous activity recorded from populations of neurons in unanesthetized mouse somatosensory cortex using in vivo two-photon Ca^{2+} imaging (data previously published in (Gonçalves et al., 2013), see Methods for experimental details). We compared the data from wild-type (WT) mice with *Frm1* KO mice, the best studied animal model for Fragile-X syndrome, across three different developmental time points: just before (P9—11) and after (P14—16) the critical period, and a more mature timepoint (P30—40). Example ΔF/F raster plots from each group are shown in Figure 4A. We binned the data into 1 s timebins (originally imaged at 4 Hz), then transformed each neuron's timeseries of ΔF/F values into a probabilistic sequence of binary ON/OFF values by assuming a Poisson firing model (Methods). We then summarized the neural population activity from each animal with three statistics: the mean ON probability across all recorded neurons (Figure 4C), the standard deviation (s.d.) in ON probability across neurons (Figure 4D), and the mean correlation between all pairs of neurons (Figure 4E). Together these measures capture both the statistics of the bulk population activity and some indication of the heterogeneity across neurons. For mean firing rates, the only change we detected was a decrease in firing probability in WT between P14—16 and P30—40 ($p = 0.027$), which was coupled with an increased s.d. of firing rates ($p = 0.015$). We also detected a higher firing rate s.d. in P9—11 KO animals than WT ($p = 0.031$). Finally, as previously reported (Golshani et al., 2009; Gonçalves et al., 2013; Rochefort et al., 2009), we found a substantial decrease in pairwise correlations in both genotypes across development, with slightly higher correlations in KO animals than WT at P9—11 ($p = 0.029$) and P14—16 ($p = 0.047$). These results are consistent with a general model where neural firing becomes desynchronized and sparsified around the critical period, at least in WT animals (Golshani et al., 2009; Rochefort et al., 2009).

For the three summary statistics from each animal, we used a gradient descent algorithm to find the five parameters of a population-level version of the logistic model that best matched the activity statistics (see Methods). For each animal, we plot the mean slope and mean threshold fits (Figure 4F) on top of the previously calculated (Figure 3C) 2D slope-threshold maps of firing rate and correlation. We find that in young animals, P9—11, most points are scattered at high values of both slope and threshold (Figure 4D left). With age, the parameter fits for both genotypes moved south-west towards the low slope and low threshold region of parameter space (Figure 4D center and right). The mean location of the cloud of points at each developmental age differed between WT and KO. We plot the direction of shift in group mean from WT to KO in Figure 4G. In young animals, P9—11 and P14—16, the KO group had both higher slope and higher threshold than WT, whereas in adult animals, P30—40, the KO group had a lower slope and lower threshold than WT. These results demonstrate an opposite direction of circuit parameter change in young Fragile-X mice compared to adults, which could not be captured by examining either neural firing rates or correlations.

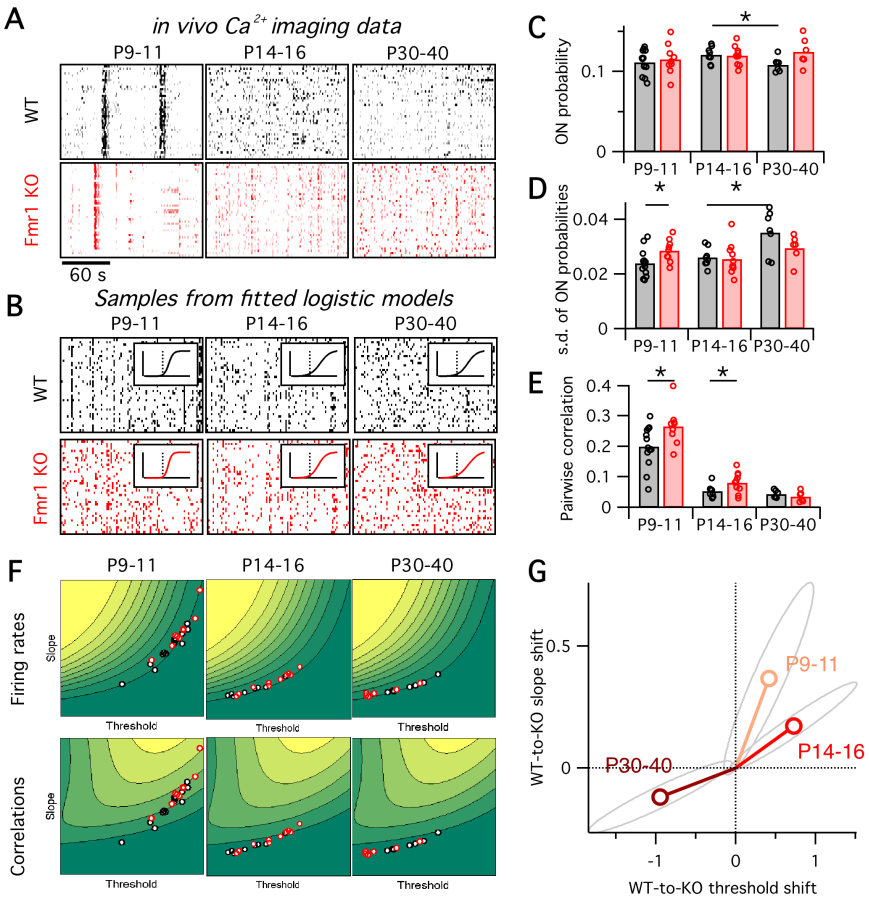

Figure 4. Fragile-X fits from logistic model.
A: Example Ca^{2+} imaging dF/F raster plots from a single animal from each of two genotypes, WT and *Frm1* KO, and three age groups, P9—11, P14—16 and P30—40. In each case 3 minutes of data are shown from 40 neurons.
B: Example samples from the fitted logistic models, corresponding to the six groups shown in panel A. Inset shows group mean fitted logistic function, dashed vertical line represents zero.
C-E: Mean firing probability (C), standard deviation of firing probabilities (D) and mean pairwise correlation across all neurons (E). Each circle represents data from a single animal, bars represent group means.
F: Fitted logistic mean slope and mean threshold values for data from each WT (black circles) and *Fmr1* KO (red circles) animal. Values overlaid on same firing rate (top) and correlation (bottom) maps from Figure 3C.
G: Shift in mean logistic slope and threshold values from WT to KO for P9—11 (orange), P14—16 (red) and P30—40 (brown). Grey ellipses represent 95% confidence intervals (Methods).

Earlier we asked how sensitive the logistic model slope and threshold parameters were to alterations in the many underlying neural circuit components (Figure 2). In a similar way, we

can also ask how sensitive the neural firing rates and correlations are to alterations in the logistic slope and threshold parameters. This is important since inspection of the 2-dimensional maps in Figure 2C shows that these sensitivities will differ depending on starting location within the slope-threshold space. To quantify this effect, we calculated the sensitivity of both the firing rate and correlations to small changes in the slope and threshold (Figure 5, see Methods), local to the fitted logistic parameter values for each animal (black and red circles in Figure 4F). Across all animals, we found that changes in the slope and threshold were qualitatively consistent but quantitatively inconsistent. Increasing the slope or decreasing the threshold always increased both firing rates and correlations. However, the magnitude of these effects depended strongly on developmental age (we found only minor differences between genotypes at any age). In young animals, P9—11, changes in the logistic threshold (solid bars in Figure 5) had substantial effects on both firing rates and correlation. This sensitivity decreased with age ($p \leq 0.013$ for firing rates, $p < 0.01$ for correlations from P9—11 to P14—16, both for pooled data across genotypes), so that in adult animals, P30-40, changes in threshold had relatively little effect on neural activity statistics. A different picture emerged for the logistic slope parameter (striped bars in Figure 5). There, the firing rate sensitivity increased with from P9—11 to P14—16 ($p < 1e\text{-}6$) (Figure 5A), while correlation sensitivity stayed approximately constant ($p \geq 0.18$) (Figure 5B). These results show that the quantitative relationships between neural activity statistics and the underlying circuit parameters are not fixed across development.

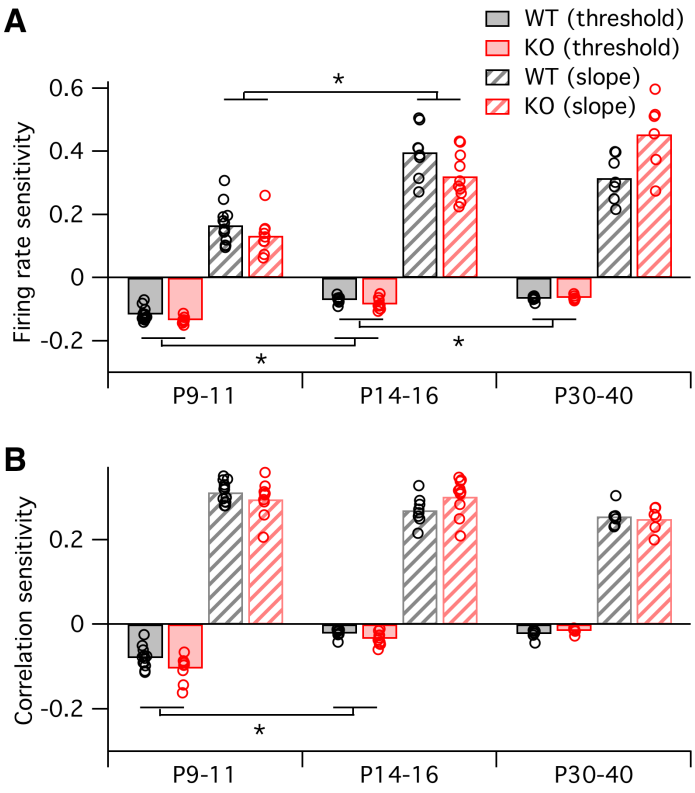

Figure 5. Sensitivity of firing rate and correlations with respect to logistic model parameters, local to the parameter fit for each animal.
Sensitivity of firing probability (**A**) and pairwise correlations (**B**) to change in threshold (solid bars) and slope (striped bars) parameters of logistic model, about the fitted parameter values for each animal (circles) displayed in Figure 4F. Bars represent group means.

What are the functional implications of these alterations in firing rates and correlations in Fragile-X mice across development? To address this, we attempted to calculate the entropy of the neural population activity for the data from each animal. Entropy is a quantity from information theory, measured in bits, that puts a hard upper bound on the amount of information that can be represented by any coding system (Cover and Thomas, 2006). Intuitively, the entropy measures how uniform the neural population activity pattern distribution is: it is large if the circuit exhibits many different activity patterns over time, and small if only a few activity patterns dominate. Entropy is an appealing measure for the present problem because it is sensitive both to neural firing rates and to correlations at all orders. It is typically highest when firing rates are high and correlations are low. Although entropy is notoriously

difficult to calculate for large neural populations because most estimation methods require impractically long data recordings (Quian Quiroga and Panzeri, 2009), we recently developed a new statistical method for this purpose, called the *population tracking model*, that scales well to large numbers of neurons, even for limited data (O'Donnell et al., in press). We fit this population tracking model to the same Ca^{2+} imaging data as analyzed above (Figure 6). An intermediate step in estimating the neural entropy involves calculating a low-parameter approximation of the entire probability distribution over all 2^N neural population activity patterns, where N is the number of neurons. The cumulatives of these probability distributions calculated for 50-neuron subsets of the recordings are shown in Figure 6A. In young animals P9—11, a small number of activity patterns accounts for a large fraction of the probability mass (Figure 6A left). For example, based on these curves, 50% of the time we would expect to see the same 1000—10,000 patterns out of a possible total $2^{50} \approx 10^{15}$ patterns. In contrast, in older animals P14—16 and P30—40 the cumulative distributions shift rightwards so that more patterns are typically observed (Figure 6A center, right). In these cases, around 1,000,000 patterns are needed to account for 50% probability mass.

Instead of attempting to quantify these shifts by asking how many patterns are needed to cross an arbitrary threshold of probability mass, we instead calculated the entropy, which takes into account the shape of the entire probability distribution. The entropy depends the number of neurons analyzed, so we normalized all estimates to calculate the entropy per neuron (Figure 6B—C). Since we are treating neurons as binary, the entropy/neuron was bounded between 0 and 1 bits. For all age groups, and for both WT and *Fmr1* KO animals, entropy/neuron progressively decreased with the number of neurons analyzed (Figure 6B). Because each imaging session captured a different number of neurons (range 40—198, median 97), we fit the entropy/neuron versus number of neurons data with a double exponential function (see Methods) and use the fit to provide a standardized estimate of the entropy/neuron for 100-neuron populations (Figure 6C). In WT animals, entropy/neuron showed a non-monotonic trajectory across development (O'Donnell et al., in press). At P9—11 it was low, 0.38 bits (95% c.i. [0.35:0.41]), before increasing at P14—16 ($p < 0.001$) to 0.50 bits (95% c.i. [0.48:0.52]), before decreasing again at P30—40 ($p = 0.028$) to 0.45 bits (95% c.i. [0.42:0.48]). We found a

different entropy trajectory in *Frm1* KO animals. There, although entropy/neuron also began low at 0.34 bits (95% c.i. [0.30:0.39]), not different from WT (p= 0.19), when it increased at P14—16 ($p < 0.001$) to 0.465 bits (95% c.i. [0.45:0.48]) it remained lower than for WT (p = 0.048). Finally, instead of decreasing as in the WT case, entropy continued to increase in P30—40 *Fmr1* KO animals (p = 0.033) to 0.51 bits (95% c.i. [0.47:0.55]), higher than WT (p = 0.034). These entropy values estimated directly from Ca^{2+} imaging data agreed well with entropy estimates for synthetic data sampled from the previously fit logistic models (Supplementary Figure 1). In summary, unlike WT animals, *Fmr1* KO mice showed a monotonically increasing entropy/neuron from P9—11 to P30—40. Furthermore, the direction of change in entropy between P14—16 and P30—40 was opposite for WT and *Fmr1* KO animals, decreasing in the former and increasing in the latter.

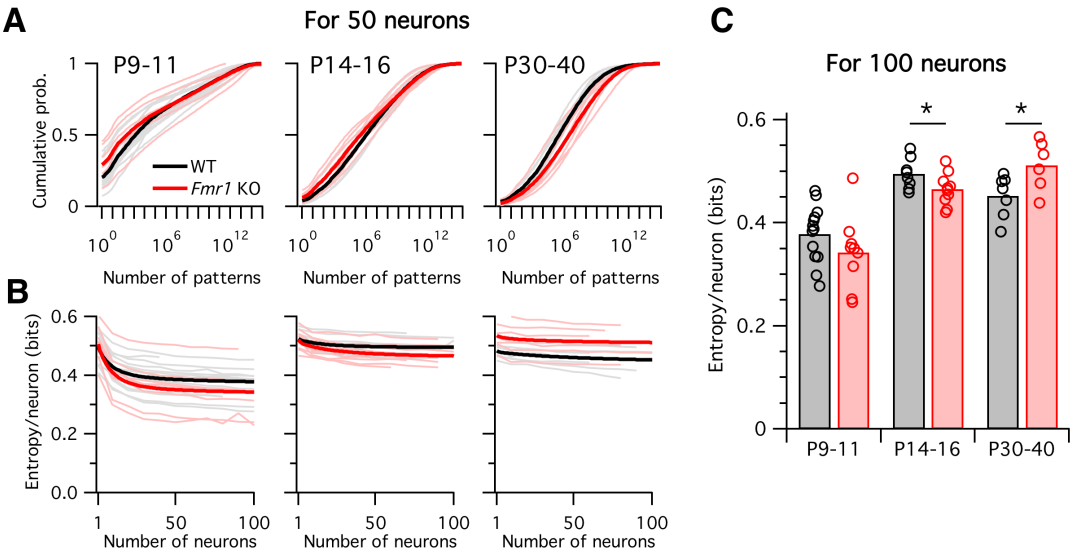

Figure 6. Differing trajectories of WT and KO entropy across development.
A: Cumulative probability mass as a function of the number of patterns. Patterns ordered from most probable to least probable. Thin lines are mean across many randomly-chosen 50-neuron subsets from a given animal, and thick lines represent means across all animals of a given genotype.
B: Entropy per neuron as a function of the number of neurons analyzed. Thin lines are mean across many randomly chosen subsets for a given animal, thick lines are group mean of double exponential fits to the data (see Methods). Age groups (left to right) are as in panel A.
C: Estimated entropy/neuron for 100 neuron populations. Circles represent individual animals, bars are group means.

Discussion

The 1-dimensional E/I imbalance model has been widely used for interpreting neural circuit changes observed in animal models of diverse brain disorders (Bateup et al., 2011; Dani et al., 2005; Gibson et al., 2008; Kehrer et al., 2008; Wallace et al., 2012). In the case of Fragile-X syndrome, the hyperexcitability prediction of the E/I imbalance model is consistent with many of the symptoms of the disease (e.g. seizures, hyperarousal, hyperactivity, hypersensitivity to sensory stimuli) and the known pathogenic defects implicated in *Fmr1* KO mice (diminished GABA signaling, exaggerated intrinsic excitability, increased neuronal firing rates; reviewed by Contractor et al., 2015). Here we combined computational modeling with analysis of *in vivo* neural activity data to ask whether the E/I model could also quantitatively account for alterations in multiple neural activity statistics. We found that this model is too simple to account for the joint alterations in neural firing rates and correlations observed in Fragile-X model mice. This suggests that future studies of brain disorders may need to consider higher-dimensional models of neural circuit dysfunction.

First, we built a detailed computational model of a specific neural circuit, L2/3 of mouse somatosensory cortex (Figure 1), and asked how sensitive the spiking responses of the overall circuit were to changes in its underlying neural components, many of which are known to be altered in *Fmr1* KO mice (Bureau et al., 2008; Gibson et al., 2008; Gonçalves et al., 2013; Harlow et al., 2010; Hays et al., 2011; Paluszkiewicz et al., 2011; Patel et al., 2013; Testa-Silva et al., 2012). We found that while changing some neural parameters did have a large effect, changing of other parameters had little or no effect on circuit function (Figure 2B). This property, termed sloppiness, has been reported as widely prevalent in computational models of biological systems (Gutenkunst et al., 2007; O'Leary et al., 2015). Its existence has two important implications for studies of brain disorders: first, many of the physiological component changes discovered in animal models may be entirely benign at the circuit level. Second, any treatment designed to correct circuit function does not necessarily need to correct all of the low-level properties in order to be successful.

In addition to the varying magnitudes of circuit components' effect on circuit function, we also found that different components shifted the circuit input-output function in different directions,

333 as defined by our 2D logistic response model (Figures 1 and 2). Even circuit parameters that
334 are nominally of the same type, such as the strength of glutamatergic synapses between
335 excitatory (E) neurons in L4 to E neurons in L2/3 or synaptic strength between E neurons
336 within L2/3, had qualitatively different effects on the circuit response to stimulation (Figure 2).
337 According to the standard E/I imbalance model (Rubenstein and Merzenich, 2003), both of
338 these parameters should have similar effects on circuit function; but according to the logistic
339 response model we studied, their differing effects on slope and threshold parameters must
340 necessarily lead to different magnitudes of change in neural firing rates and correlations
341 (Figure 3C). Indeed, no 1-dimensional model of circuit function could ever capture the
342 heterogeneity in parameter sensitivities that we observed (Figure 2B).

343 Next, we fit the parameters of the logistic response model to match the *in vivo* firing statistics of
344 neural populations from WT and *Fmr1* KO mice of varying age (Figure 4). Previous studies had
345 found that neural correlations decrease during development (Golshani et al., 2009; Rochefort
346 et al., 2009), and that *Fmr1* KO mice had higher correlations and firing rates than WT mice at
347 P14–16 (Gonçalves et al., 2013; La Fata et al., 2014). A recent study suggests circuit
348 hypersynchrony is also found in different mouse models of Rett syndrome (Lu et al., 2016).
349 However, the relationship between these changes in firing statistics and the underlying neural
350 circuit components were unclear. Our logistic model helps bridge this gap, leading to two
351 findings: first, the direction of circuit parameter change from young (P9—11 and P14—16) to
352 mature (P30—40) animals is opposite in WT to KO mice (Figure 4G). Similar opposing
353 switches in sensory cortex properties with age were also recently reported in *Frm1* KO rats
354 (Berzhanskaya et al., 2016). Second, we found that the sensitivity of neural firing rates and
355 correlations to changes in underlying circuit components depends on developmental age
356 (Figure 5). Taken together, these findings imply that qualitatively different interventions may be
357 needed at different stages of development in Fragile-X, and perhaps other
358 neurodevelopmental disorders, to shift cortical circuit function towards typical wild-type
359 operation.

360 Spontaneous, intrinsic activity is ubiquitously present in mammalian cerebral cortex. It is highly
361 structured at multiple spatiotemporal scales (Mitra et al., 2015; Ringach, 2009) and interacts

362 strongly with the signals evoked by sensory stimulation (Ringach, 2009). Cellular-resolution
363 recordings in animals have shown that the patterns of spontaneous activity in neural
364 populations are representative of the ensemble of activity patterns used by the brain to
365 represent sensory stimuli (Berkes et al., 2011; Luczak et al., 2009; Miller et al., 2014). Here we
366 found that the entropy of spontaneous activity in WT mouse somatosensory cortex follows an
367 inverted-U shaped trajectory across development, and that this trajectory is dramatically
368 altered in the *Fmr1* KO mouse model of Fragile-X (Figure 6). Although we saw no reliable
369 differences across genotypes in early postnatal animals (P9—11), *Fmr1* KO animals showed
370 lower entropy than WT after the second postnatal week (P14—16), while surprisingly switching
371 to show higher entropy than WT in adult (P30—40). Notably, this switch in the direction of
372 entropy change from WT to KO during development mirrors the reversing we saw in logistic
373 model parameter changes in Figure 4G. Together, these findings suggest a perturbed
374 trajectory of cortical development during the critical period in *Fmr1* KO mice (Meredith et al.,
375 2012). However, our results cannot distinguish whether the observed perturbation in L2/3
376 activity statistics reflects a developmental delay, or a permanently altered developmental
377 trajectory. Further studies at later developmental time points are needed.

378 What is the functional significance of these shifts in population entropy? Previous work
379 suggested that the entropy of neural circuit activity may be optimally tuned at intermediate
380 levels as a trade-off between maximizing representational capacity at high entropy, versus
381 maintaining error correction and regularization at low entropy (Schneidman et al., 2006). These
382 properties can also be thought of as trading off between discrimination and generalization,
383 respectively (Qian and Lipkin, 2011). If we assume that WT mice are optimally tuned, our
384 findings predict that young *Fmr1* KO mice should show poorer somatosensory discrimination in
385 behavioral tasks than wild-type animals, while in contrast adult *Fmr1* KO mice should perform
386 more poorly on tasks involving generalization across somatosensory stimuli.

387 If the 1-dimensional E/I imbalance model is not sufficiently rich to capture the circuit changes
388 observed in neurodevelopmental disorders, what should it be replaced with? How many
389 dimensions or degrees of freedom should a working model for a brain disorder have? We
390 suggest that the most promising approach is to start by considering the computational function

of a particular neural circuit, then working backwards to design a model that is both sophisticated enough to capture the key information processing features of the circuit, but simple enough to interpret and link to physiological data. In this study we considered a 2-parameter model of L2/3 somatosensory cortex's input-output function, which could account for both neural firing rates and correlations. Other brain circuits may demand models with more degrees of freedom. Crucially, the most informative models need not be those that include the highest level of physiological detail. All models are ultimately wrong in the sense that they make abstractions about their underlying parts, and detailed models carry the additional burden of fitting many parameters, which may be difficult to adequately constrain (O'Leary et al., 2015).

One potential use of simple parametric circuit models such as the ones we employed here may be as a tool for rationally designing candidate intervention compounds and then screening their effects on neural population activity. This approach could complement the traditional strategy of designing drugs based on reversing molecular deficits and then assessing the drug's impact on animal model behavior. Indeed, our results suggest that given the multi-dimensionality of circuit properties, it may prove difficult or impossible to find a single compound that can correctly reverse deficits at any age. This scenario might require a combination of drugs chosen to push circuit-level properties towards the 'correct' region of parameter space. The framework we have introduced in this study can facilitate this type of high-dimensional intervention analysis for diverse neurodevelopmental disorders.

Methods

Mouse in vivo calcium imaging recording

All Ca^{2+} imaging data were published previously (Gonçalves et al., 2013). Briefly, data were collected from male and female C57Bl/6 wild-type mice at P9–40. Mice were anesthetized with isoflurane, and a cranial window was fitted over primary somatosensory cortex by stereotaxic coordinates. Mice were then transferred to a two-photon microscope and headfixed to the stage while still under isoflurane anesthesia. 2—4 injections of the Ca^{2+} sensitive Oregon-

419 Green BAPTA-1 (OGB) dye and sulforhodamine-101 (to visualize astrocytes) were injected
420 200 um below the dura. Calcium imaging was performed using a Ti-Sapphire Chameleon Ultra
421 II laser (Coherent) tuned to 800 nm. Imaging in unanesthetized mice began within 30-60 mins
422 of stopping the flow of isoflurane after the last OGB injection. Images were acquired using
423 ScanImage software (Pologruto et al., 2004) written in MATLAB (MathWorks). Whole-field
424 images were collected using a 20× 0.95 NA objective (Olympus) at an acquisition speed of 3.9
425 Hz (512 × 128 pixels). Several 3-minute movies were concatenated and brief segments of
426 motion artifacts were removed (always <10 s total). Data were corrected for x—y drift. Cell
427 contours were automatically detected and the average ΔF/F signal of each cell body was
428 calculated at each time point. Each ΔF/F trace was low-pass filtered using a Butterworth filter
429 (coefficient of 0.16) and deconvolved with a 2 s single-exponential kernel (Yaksi and Friedrich,
430 2006). To remove baseline noise, the standard deviation of all points below zero in each
431 deconvolved trace was calculated, multiplied by two, and set as the positive threshold level
432 below which all points in the deconvolved trace were set to zero. Estimated firing rates of the
433 neurons, r_i(t), were then obtained by multiplying the deconvolved trace by a factor previously
434 derived empirically from cell-attached recordings in vivo (Golshani et al., 2009).

435 **Computational methods**

436 Data analysis and logistic model calculations were done using MATLAB (Mathworks).

437 **Detailed layer 2/3 model simulations**

438 Layer 2/3 model simulations (Figures 1 and 2) were implemented with the Python-based
439 simulator Brian (http://briansimulator.org/) (Goodman and Brette, 2009), and results analyzed
440 with MATLAB (Mathworks). The model consisted of four populations of reciprocally connected
441 leaky integrate-and-fire neurons representing a L2/3 somatosensory barrel circuit: 1700
442 excitatory neurons, 70 PV inhibitory neurons, 115 $5HT_{3A}R$ inhibitory neurons, and 45 SOM
443 inhibitory neurons, driven by a separate population of 1500 excitatory spike sources
444 representing input from L4. Cell numbers were estimated by combining layer-specific excitatory
445 and inhibitory cell count information from Lefort et al. (2009) with the approximate percentages
446 of the three inhibitory cell groups given by Petersen and Crochet (2013). All synaptic
447 connections were formed probabilistically by drawing independent random Bernoulli variables

448 with connection type-specific probabilities. Synaptic PSP amplitudes were drawn
449 independently for each synapse from a log-normal distribution constrained by the
450 experimentally reported mean and median values for each particular connection type.
451 Synapses in the model were conductance-based, but since synaptic strengths reported in the
452 literature were typically in terms of EPSP/IPSP amplitude, in accordance with how the
453 experiments were performed (Avermann et al., 2012), we set each maximal synaptic
454 conductance as the value needed to generate a PSP of the desired amplitude when the target
455 neuron started at resting potential in the case of EPSPs or -55mV in the case of IPSPs, which
456 we computed analytically. Refractory periods were calculated as the inter-spike-interval
457 corresponding to the maximal experimentally reported firing rate. Release probability and
458 synaptic strength values for unconnected neurons are excluded from Table 1. Excitatory
459 synaptic time constants were set at 2 ms, which is typical for the fast component of AMPA
460 receptor responses, but could not be estimated from the PSP statistics in Avermann et al.
461 (2012) because of masking by the slower membrane time constant. The mathematical form of
462 our model meant that inhibitory synaptic time constants needed to be equal for all incoming
463 inhibitory synapses to a neuron. We set these to 40 ms for E, $5HT_{3A}R$ and SOM neurons and
464 16 ms for PV neurons, which were the typical values of the IPSP decay time constants in the
465 Avermann et al. (2012) dataset. Due to lack of direct data for this circuit, connection
466 probabilities for synapses from L4 E neurons to E, PV and SOM L2/3 neurons was set to a
467 typical cortical value of 0.15, while $5HT_{3A}R$ neurons did not receive any input from L4 (Gentet
468 et al., 2012). Similarly due to a lack of direct data, we set synaptic release probabilities for
469 connections from L4 to L2/3 neurons to a typical cortical value of 0.25, while mean and median
470 L4 excitatory PSP amplitudes onto L2/3 PV and SOM were set to 0.8 and 0.48 mV,
471 respectively, to match reported data for L4 EPSP amplitudes onto L2/3 E neurons (Lefort et al.,
472 2009). L4 neuron dynamics were not explicitly simulated, but instead modeled only as a set of
473 output spike trains. After selecting the subset of active L4 neurons (see Results), spike times
474 were drawn randomly from a Gaussian distribution with standard deviation of 2 ms.

475 For the simulations presented in Figure 2 we varied only 76 model parameters, which is 24
476 less than the total number of 100 model parameters listed in Table 1. We excluded the four

477 neuronal refractory periods (because in almost all simulations each neuron spiked a maximum
478 of once, making the refractory period irrelevant), and the six connection probabilities that were
479 fixed at zero. Finally, we grouped together the mean and median PSP amplitudes for each of
480 the fourteen non-zero synaptic connections, so that both parameters were increased or
481 decreased by the same fraction in tandem. Together these choices reduced the number of test
482 parameters from 100 to 76.

483 For all parameters that naturally range from 0 upwards, such as the number of neurons or
484 release probability, we increased or decreased their values during testing in the most intuitive
485 way, by adding +/- 20% of the baseline value. However, this method was less useful for other
486 parameters, such as cell resting voltage, for which we reasoned it made more sense to scale
487 relative to another parameter, such as spike threshold. As a result, we varied 1) resting voltage
488 relative to its difference from spike threshold; 2) spike threshold relative to its difference with
489 resting voltage; 3) excitatory synaptic reversal potentials relative to resting voltage; 4) inhibitory
490 synaptic reversal potentials relative to spike threshold.

Table 1. L2/3 computational circuit model parameters and mean slope & threshold shifts.

Parameter	Value	Source	+20% effect on slope, thresh	Parameter	Value	Source	+20% effect on slope, thresh
N_E	1700	[1]	slope: 6.4 x10^{-3} thresh: 5.16	$pcon_{I5htE}$	0.465	[2]	slope: -3.25 x10^{-3} thresh: -0.103
N_{Ipv}	70	[1]	slope: 4.3 x10^{-3} thresh: -1.51	$pcon_{I5htIpv}$	0.38	[2]	slope: -7.13 x10^{-3} thresh: -0.298
N_{I5ht}	115	[1]	slope: -0.0104 thresh: -0.58	$pcon_{I5htI5ht}$	0.38	[2]	slope: 6.07 x10^{-4} thresh: 0.175
N_{Isom}	45	[1]	slope: -0.001 thresh: -0.83	$pcon_{I5htIsom}$	0	No data	Not tested
N_{EL4}	1500	[1]	slope: -0.106 thresh: 3.43	$pcon_{IsomE}$	0.5	[5]	slope: -6.29 x10^{-3} thresh: -0.8919
$Vrest_E$	-68 mV	[2]	slope: 0.049 thresh: -6.09	$pcon_{IsomIpv}$	0	No data	Not tested
$Vrest_{Ipv}$	-68 mV	[2]	slope: -0.016 thresh: -0.963	$pcon_{IsomI5ht}$	0	No data	Not tested
$Vrest_{I5ht}$	-62 mV	[2]	slope: -9.48 x10^{-4} thresh: 0.205	$pcon_{IsomIsom}$	0	No data	Not tested
$Vrest_{Isom}$	-57 mV	[3]	slope: 3.58 x10^{-3} thresh: 0.034	$prel_{EL4E}$	0.25	No data	slope: -0.112 thresh: 4.21
Vth_E	-38 mV	[2]	slope: -3.76 x10^{-3} thresh: -0.381	$prel_{EL4Ipv}$	0.25	No data	slope: 0.0103 thresh: 0.682
Vth_{Ipv}	-37.4 mV	[2]	slope: 3.87 x10^{-3} thresh: 0.221	$prel_{EL4Isom}$	0.25	No data	slope: -2.06 x10^{-3} thresh: -0.537
Vth_{I5ht}	-36 mV	[2]	slope: -1.12 x10^{-3} thresh: 0.013	$prel_{EE}$	0.25	No data	slope: 4.99 x10^{-3} thresh: 6.074
Vth_{Isom}	-40 mV	[3]	slope: -3.26 x10^{-3} thresh: -0.083	$prel_{EIpv}$	0.25	No data	slope: -4.04 x10^{-4} thresh: 0.163

Rin_{E}	160 MΩ	[2]	slope: 1.95 x10^{-3} thresh: -0.283	$prel_{EI5ht}$	0.25	No data	slope: -9.32 x10^{-3} thresh: -0.532
Rin_{Ipv}	100 MΩ	[2]	slope: -8.38 x10^{-3} thresh: -0.283	$prel_{EIsom}$	0.25	No data	slope: -7.32 x10^{-3} thresh: -0.3847
Rin_{I5ht}	200 MΩ	[2]	slope: -3.87 x10^{-3} thresh: -0.653	$prel_{IpvE}$	0.25	No data	slope: 1.03 x10^{-2} thresh: -0.941
Rin_{Isom}	250 MΩ	[4]	slope: 7.55 x10^{-3} thresh: 0.465	$prel_{IpvIpv}$	0.25	No data	slope: 1.21 x10^{-3} thresh: -0.061
τm_{E}	28 ms	[2]	slope: -9.59 x10^{-3} thresh: 0.268	$prel_{IpvI5ht}$	0.25	No data	slope: -4.73 x10^{-3} thresh: 0.011
τm_{Ipv}	21 ms	[2]	slope: 4.82 x10^{-3} thresh: 0.027	$prel_{I5htE}$	0.25	No data	slope: -1.63 x10^{-3} thresh: -0.379
τm_{I5ht}	10 ms	[2]	slope: -5.09 x10^{-3} thresh: -0.302	$prel_{I5htIpv}$	0.25	No data	slope: -3.41 x10^{-3} thresh: -0.262
τm_{Isom}	30 ms	[4]	slope: -2.89 x10^{-3} thresh: -0.159	$prel_{I5htI5ht}$	0.25	No data	slope: 3.05 x10^{-3} thresh: 0.123
$tref_{E}$	55.5 ms	[2]	Not tested	$p_{rel,IsomE}$	0.25	No data	slope: -2.13 x10^{-4} thresh: -0.65
$tref_{Ipv}$	5.4 ms	[2]	Not tested	$w_{EL4E,mean}$	0.8 mV	[1]	slope: -0.142 thresh: 0.342
$tref_{I5ht}$	21.3 ms	[2]	Not tested	$w_{EL4E,median}$	0.48 mV	[1]	slope: -0.142 thresh: 0.342
$tref_{Isom}$	20 ms	[3]	Not tested	$w_{EL4Ipv,mean}$	0.8 mV	$=w_{EL4E}$	slope: 3.61 x10^{-3} thresh: 6.54 x10^{-3}
$\tau syn_{E,e}$	2 ms	Typical	slope: 1.37 x10^{-2} thresh: -1.79	$w_{EL4Ipv,median}$	0.48 mV	$=w_{EL4E}$	slope: 3.61 x10^{-3} thresh: 6.54 x10^{-3}
$\tau syn_{E,i}$	40 ms	[2]	slope: -7.29 x10^{-3} thresh: 0.48	$w_{EL4Isom,mean}$	0.8 mV	$=w_{EL4E}$	slope: 5.05 x10^{-3} thresh: -0.329
$\tau syn_{Ipv,e}$	2 ms	Typical	slope: -9.79 x10^{-3} thresh: -0.477	$w_{EL4Isom,median}$	0.48 mV	$=w_{EL4E}$	slope: 5.05 x10^{-3} thresh: -0.329
$\tau syn_{Ipv,i}$	16 ms	[2]	slope: 1.56 x10^{-3} thresh: -0.097	$w_{EE,mean}$	0.37 mV	[2]	slope: 7.44 x10^{-3} thresh: 5.34
$\tau syn_{I5ht,e}$	2 ms	Typical	slope: 4.52 x10^{-3} thresh: -0.047	$w_{EE,median}$	0.2 mV	[2]	slope: 7.44 x10^{-3} thresh: 5.34
$\tau syn_{I5ht,i}$	40 ms	[2]	slope: -3.82 x10^{-3} thresh: -0.387	$w_{EIpv,mean}$	0.82 mV	[2]	slope: -3.77 x10^{-4} thresh: -0.297
$\tau syn_{Isom,e}$	2 ms	Typical	slope: -0.0126 thresh: -8.82 x10^{-3}	$w_{EIpv,median}$	0.68 mV	[2]	slope: -3.77 x10^{-4} thresh: -0.297
$\tau syn_{Isom,i}$	40 ms	[2]	slope: -4.88 x10^{-3} thresh: -0.301	$w_{EI5ht,mean}$	0.39 mV	[2]	slope: -6.81 x10^{-3} thresh: -0.46
$Erev_{e}$	0 mV	Typical	slope: -0.056 thresh: 1.53	$w_{EI5ht,median}$	0.19 mV	[2]	slope: -6.81 x10^{-3} thresh: -0.46
$Erev_{Ei}$	-68 mV	$=Vrest_{E}$	slope: 3.2x10^{-3} thresh: -3.77	$w_{EIsom,mean}$	0.5 mV	No data	slope: -3.61 x10^{-3} thresh: -0.359
$Erev_{Ipvi}$	-68 mV	$=Vrest_{Ipv}$	slope: -0.010 thresh: -0.617	$w_{EIsom,median}$	0.4 mV	No data	slope: -3.61 x10^{-3} thresh: -0.359
$Erev_{I5hti}$	-62 mV	$=Vrest_{I5ht}$	slope: 3.8x10^{-3} thresh: 0.132	$w_{IpvE,mean}$	0.52 mV	[2]	slope: 6.41 x10^{-3} thresh: -1.47
$Erev_{Isomi}$	-57 mV	$=Vrest_{Isom}$	slope: -4.2x10^{-3} thresh: -0.088	$w_{IpvE,median}$	-0.29 mV	[2]	slope: 6.41 x10^{-3} thresh: -1.47
$pcon_{EL4E}$	0.15	No data	slope: -0.121 thresh: 2.99	$w_{IpvIpv,mean}$	-0.56 mV	[2]	slope: -2.52 x10^{-3} thresh: -0.345
$pcon_{EL4Ipv}$	0.15	No data	slope: 1.38x10^{-3} thresh: 0.029	$w_{IpvIpv,median}$	-0.44 mV	[2]	slope: -2.52 x10^{-3} thresh: -0.345
$pcon_{EL4I5ht}$	0	No data	Not tested	$w_{IpvI5ht,mean}$	-0.83 mV	[2]	slope: -4.24 x10^{-3} thresh: -0.266
$pcon_{EL4Isom}$	0.15	No data	slope: 7.62 x10^{-3} thresh: -0.245	$w_{IpvI5ht,median}$	-0.6 mV	[2]	slope: -4.24 x10^{-3} thresh: -0.266

$pcon_{EE}$	0.17	[2]	slope: 5.86 x10^{-3} thresh: 6.084	$w_{I5htE,mean}$	-0.49 mV	[2]	slope: -3.61 x10^{-4} thresh: -0.018
$pcon_{EIpv}$	0.575	[2]	slope: -1.17 x10^{-3} thresh: -0.099	$w_{I5htE,median}$	-0.3 mV	[2]	slope: -3.61 x10^{-4} thresh: -0.018
$pcon_{EI5ht}$	0.24	[2]	slope: -6.44 x10^{-3} thresh: -0.541	$w_{I5htIpv,mean}$	-0.49 mV	[2]	slope: -1.77 x10^{-3} thresh: -0.187
$pcon_{EIsom}$	0.5	[5]	slope: -4.37 x10^{-3} thresh: -0.27	$w_{I5htIpv,median}$	-0.15 mV	[2]	slope: -1.77 x10^{-3} thresh: -0.187
$pcon_{IpvE}$	0.6	[2]	slope: 7.16 x10^{-3} thresh: -1.049	$w_{I5htI5ht,mean}$	-0.37 mV	[2]	slope: -4.12 x10^{-3} thresh: -0.416
$pcon_{IpvIpv}$	0.55	[2]	slope: -2.61 x10^{-3} thresh: -0.0456	$w_{I5htI5ht,median}$	-0.23 mV	[2]	slope: -4.12 x10^{-3} thresh: -0.416
$pcon_{IpvI5ht}$	0.24	[2]	slope: -2.81 x10^{-3} thresh: -0.458	$w_{IsomE,mean}$	-0.5 mV	No data	slope: -0.013 thresh: -0.984
$pcon_{IpvIsom}$	0	No data	Not tested	$w_{IsomE,median}$	-0.4 mV	No data	slope: -0.013 thresh: -0.984

Source [1] is Lefort et al. (2009), [2] is Avermann et al. (2012), [3] is Fanselow et al. (2008), [4] is Kinnischtzke et al. (2012), [5] is Fino and Yuste (2011). *N* is number of neurons, *Vrest* is resting potential, *Vth* is spike voltage threshold, *Rin* is input resistance, *tref* is refractory period, *τm* is the membrane time constant, *τsyn* is the synaptic time constant with the first subscript indicating the postsynaptic neuron type and the second subscript the neurotransmitter type of the presynaptic neuron (*e* or *i*), *Erev* is the synaptic reversal potential, *pcon* is the synaptic connection probability, *prel* is the synaptic release probability, *w* is the mean or median post-synaptic potential amplitude as indicated. For all neuronal parameters, the subscript indicates the neuron type: *E* is L2/3 excitatory neurons, *Ipv* is PV neurons, *I5ht* is $5HT_{3A}R$ neurons, *Isom* is SOM neurons, and *EL4* is L4 excitatory neurons. For synaptic parameters, the first and second subscripts indicate the pre- and post-synaptic neuron types, respectively.

Logistic model

From the L2/3 circuit model simulations, we numerically estimated the probability *q* that each neuron in the model fires a spike as a function of the fraction of L4 inputs that were active, *f*. We then used the generalized linear model regression tool in MATLAB to find the best fit of the two logistic model parameters for each neuron:

$$q(f) = \frac{1}{1+\exp\left(-\beta(f-f_{1/2})\right)} \quad ,$$

where the parameter β represents the slope, and the parameter $f_{1/2}$ represents the fraction of active L4 neurons at which the response probability $q = 0.5$. For clarity of presentation, in the main text we converted this $f_{1/2}$ parameter to what we termed the 'threshold', f_{thresh}, which we defined as the fraction of L4 neurons needed to reach a specified spike probability, q_{thresh}.

Throughout the study we fixed $q_{thresh} = 0.01$. The threshold is related to $f_{1/2}$ via the inverse of the logistic function

$$f_{thresh} = f_{1/2} + \log\left(\frac{q_{thresh}}{1-q_{thresh}}\right)/\beta.$$

We computed firing rates and pairwise correlations from the logistic model (Figures 3—4) in the following way. First, we assumed that the fraction of active L4 neurons is described by a normally distributed random variable with zero mean and unit variance:

$$p(f) = \frac{\exp\left(-f^2/2\right)}{\sqrt{2\pi}} = \mathcal{N}(0,1) \quad .$$

We defined the β and $f_{1/2}$ parameters relative to the mean and standard deviation of the input distribution. Since *q* is a monotonically increasing function of *f*, the probability distribution for *q* is

$$p(q) = p(f(q))\left|\frac{df}{dq}\right|$$

where $f(q)$ is the inverse of the logistic function $q(f)$ and

$\frac{df}{dq} = \frac{\left(\exp\left(-\beta\left(f-f_{1/2}\right)\right)+1\right)^2}{\beta\exp\left(-\beta\left(f-f_{1/2}\right)\right)}$. We calculate a neuron's mean firing rate μ as the expectation of *q*,

$$\mu = \mathbb{E}[q] = \int_0^1 [q \times p(q)]dq = \int_0^1 \left[q \times p(f(q))\left|\frac{df}{dq}\right|\right] dq.$$

We calculate the pairwise covariance of two homogeneous neurons driven by a common input *f* as

$\mathrm{cov} = \mathbb{E}[q^2] - (\mathbb{E}[q])^2 = \mathbb{E}[q^2] - \mu^2 = \int_0^1 \left[q^2 \times p\left(f(q)\right)\left|\frac{df}{dq}\right|\right] dq - \mu^2$, then find the pairwise correlation by normalizing the covariance by the neurons' shared variance, $\mathrm{var} = \mu(1-\mu)$.

For fitting the logistic model to the recorded neural firing rates and correlations (Figure 4), we considered a population model where the joint probability distribution across threshold and slope was specified by a 2D Gaussian, which has five parameters: threshold mean and s.d., slope mean and s.d., and slope-threshold correlation. The three constraint statistics we considered from the neural population data were the mean neural ON probability, the s.d. of neural ON probabilities, and the mean pairwise correlations. We found the best-fit model parameters for each dataset using stochastic gradient descent. We checked for fit convergence by sampling a large number of logistic model parameters from the fitted 2D

537 Gaussian, drawing binary samples from these logistic 'neurons' and computing the ON
538 probability mean and s.d., and mean pairwise correlation from the synthetic binary samples,
539 and comparing the computed statistical values to the original data statistics. For the sensitivity
540 analysis presented in Figure 5, we numerically computed the partial derivative in mean firing
541 rate and pairwise correlation with respect to the mean slope and mean threshold parameters in
542 the population logistical model, using standard finite difference methods.

543 ***Statistical tests***

544 To avoid parametric assumptions, all statistical tests were done using standard bootstrapping
545 methods with custom-written MATLAB scripts. For example when assessing the observed
546 difference between two group means $\Delta\mu_{obs}$ we performed the following procedure to calculate
547 a p-value. First we pool the data points from the two groups to create a null set S_{null}. We then
548 construct two hypothetical groups of samples S_1 and S_2 from this by randomly drawing n_1 and
549 n_2 samples with replacement from S_{null}, where n_1 and n_2 are the number of data points in the
550 original groups 1 and 2 respectively. We take the mean of both hypothetical sets $\Delta\mu_1$ and $\Delta\mu_2$
551 and calculate their difference $\Delta\mu_{null} = \Delta\mu_1 - \Delta\mu_2$. We then repeat the entire procedure 10^7
552 times to build up a histogram of $\Delta\mu_{null}$. This distribution is always centered at zero. After
553 normalizing, this can be interpreted as the probability distribution $f(\Delta\mu_{null})$ for observing a group
554 mean difference of $\Delta\mu_{null}$ purely by chance if the data were actually sampled from the same
555 null distribution. Then the final p-value for the probability of finding a group difference of at
556 least $\Delta\mu_{obs}$ in either direction is given by $p = \int_{-\infty}^{-\Delta\mu_{obs}} f(\Delta\mu_{null})d\Delta\mu_{null} + \int_{\Delta\mu_{obs}}^{\infty} f(\Delta\mu_{null})d\Delta\mu_{null}$.

557 ***Conversion from firing rate to ON/OFF probabilities for Ca^{2+} imaging data***

558 For the Ca^{2+} imaging data, we began with estimated firing rate time series $r_i(t)$ for each neuron
559 *i* recorded as part of a population of *N* neurons. For later parts of the analysis we needed to
560 convert these firing rates to binary ON/OFF values. This conversion involves a choice. One
561 option would be to simply threshold the data, but this would throw away information about the
562 magnitude of the firing rate. We instead take a probabilistic approach where rather than
563 deciding definitively whether a given neuron was ON or OFF in a given time bin, we calculate
564 the probability that the neuron was ON or OFF by assuming that neurons fire action potentials

565 according to an inhomogeneous Poisson process with rate r_i(t). The mean number of spikes
566 $\lambda_i(t)$ expected in a time bin of width Δt is $\lambda_i(t) = r_i(t)\Delta t$. We choose Δt = 1 second. Under the
567 Poisson model the actual number of spikes m in a particular time bin is a random variable that
568 follows the Poisson distribution $P(m=k) = \lambda^k \exp(-\lambda) / k!$. We considered a neuron active (ON) if
569 it is firing one or more spikes in a given time bin. Hence the probability that a neuron is ON is
570 $p_{on}(t)=1-P(m=0)=1-\exp(\lambda)$. This approach has two advantages over thresholding: 1) it
571 preserves some information about the magnitude of firing rates, and 2) it acts to regularize the
572 probability distribution for the number of neurons active by essentially smoothing nearby values
573 together.

574 ***Entropy estimation for large numbers of neurons***

575 Entropy was estimated by fitting a statistical model we recently developed, called the
576 population tracking model (O'Donnell et al., in press), to the binarized Ca^{2+} imaging data.
577 Briefly, the population tracking model fits two aspects of the data: the probability distribution for
578 the number of neurons synchronously active in the population, and also the conditional firing
579 probability that each individual neuron is active given the population count. Hence the model
580 captures both some aggregate statistics of the population activity, and some aspects of the
581 heterogeneity across neurons. See O'Donnell et al., (in press) for complete details and
582 validation of the method. Code for fitting the model to data is available at
583 https://github.com/cianodonnell/PopulationTracking.

584 The entropy/neuron generally decreased with the number of neurons considered as result of
585 the population correlations (Figure 6B), so we needed to control for neural population size
586 when comparing data from different experimental groups. On the one hand, we would like to
587 study as large a number of neurons as possible, because we expect the effects of collective
588 network dynamics to be stronger for large population sizes and this may be the regime where
589 differences between the groups emerge. On the other hand, our recording methods allowed us
590 to sample only typically around ~100 neurons at a time, and as few as 40 neurons in some
591 animals. Hence we proceeded by first estimating the entropy/neuron in each animal by
592 calculating the entropy of random subsets of neurons of varying size from 10 to 100 (if
593 possible) in steps of 10. For each population size we sampled a large number of independent

subsets, calculated the entropy of each. Finally, for each dataset we fit a double exponential function to the estimated entropy/neuron as a function of the number of neurons: $H/N = A^*\exp(-b^*N) + C^*\exp(-d^*N) + e$, and used this fit to estimate H/N for 100 neurons.

Acknowledgements

We thank Timothy O'Leary, Hannes Saal, and Alex Williams for comments on earlier versions of the manuscript. This study was supported by funding from FRAXA Research Foundation, Howard Hughes Medical Institute, Sloan-Swartz Foundation, the Dana Foundation, and the NIH (NICHD R01HD054453 and NINDS RC1NS068093).

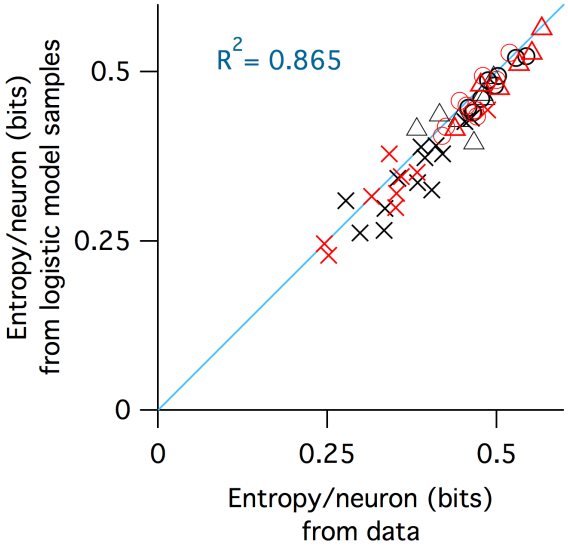

Supp Fig 1. Agreement between entropy estimated from raw data and entropy estimated from samples from fitted logistic models. Black symbols are WT, red are KO. Crosses are P9—11, circles P14—16, triangles P30—40. Blue line is identity, the R^2 value of which is reported in the inset.

603 **References**

604 Avermann, M., Tomm, C., Mateo, C., Gerstner, W., Petersen, C.C.H., 2012. Microcircuits of
605 excitatory and inhibitory neurons in layer 2/3 of mouse barrel cortex. J Neurophysiol 107,
606 3116–3134. doi:10.1152/jn.00917.2011
607 Bateup, H.S., Takasaki, K.T., Saulnier, J.L., Denefrio, C.L., Sabatini, B.L., 2011. Loss of Tsc1
608 in vivo impairs hippocampal mGluR-LTD and increases excitatory synaptic function. J
609 Neurosci 31, 8862–8869. doi:10.1523/JNEUROSCI.1617-11.2011
610 Berkes, P., Orbán, G., Lengyel, M., Fiser, J., 2011. Spontaneous cortical activity reveals
611 hallmarks of an optimal internal model of the environment. Science 331, 83–87.
612 doi:10.1126/science.1195870
613 Berzhanskaya, J., Phillips, M.A., Shen, J., Colonnese, M.T., 2016. Sensory hypo-excitability in
614 a rat model of fetal development in Fragile X Syndrome. Sci Rep 6, 30769.
615 doi:10.1038/srep30769
616 Braat, S., Kooy, R.F., 2015. The GABAA Receptor as a Therapeutic Target for
617 Neurodevelopmental Disorders. Neuron 86, 1119–1130. doi:10.1016/j.neuron.2015.03.042
618 Bureau, I., Shepherd, G.M.G., Svoboda, K., 2008. Circuit and plasticity defects in the
619 developing somatosensory cortex of FMR1 knock-out mice. J Neurosci 28, 5178–5188.
620 doi:10.1523/JNEUROSCI.1076-08.2008
621 Clancy, K.B., Schnepel, P., Rao, A.T., Feldman, D.E., 2015. Structure of a single whisker
622 representation in layer 2 of mouse somatosensory cortex. J Neurosci 35, 3946–3958.
623 doi:10.1523/JNEUROSCI.3887-14.2015
624 Contractor, A., Klyachko, V.A., Portera-Cailliau, C., 2015. Altered Neuronal and Circuit
625 Excitability in Fragile X Syndrome. Neuron 87, 699–715. doi:10.1016/j.neuron.2015.06.017
626 Cover, T.M., Thomas, J.A., 2006. Elements of Information Theory, 2nd ed. Wiley-Interscience.
627 Cruz-Martin, A., Crespo, M., Portera-Cailliau, C., 2010. Delayed Stabilization of Dendritic
628 Spines in Fragile X Mice. J Neurosci 30, 7793–7803. doi:10.1523/JNEUROSCI.0577-
629 10.2010
630 Dani, V.S., Chang, Q., Maffei, A., Turrigiano, G.G., Jaenisch, R., Nelson, S.B., 2005. Reduced
631 cortical activity due to a shift in the balance between excitation and inhibition in a mouse
632 model of Rett syndrome. Proc. Natl. Acad. Sci. U.S.A. 102, 12560–12565.
633 doi:10.1073/pnas.0506071102
634 Fanselow, E.E., Richardson, K.A., Connors, B.W., 2008. Selective, state-dependent activation
635 of somatostatin-expressing inhibitory interneurons in mouse neocortex. J Neurophysiol 100,
636 2640–2652. doi:10.1152/jn.90691.2008
637 Fino, E., Yuste, R., 2011. Dense inhibitory connectivity in neocortex. Neuron 69, 1188–1203.
638 doi:10.1016/j.neuron.2011.02.025
639 Gentet, L.J., Kremer, Y., Taniguchi, H., Huang, Z.J., Staiger, J.F., Petersen, C.C.H., 2012.
640 Unique functional properties of somatostatin-expressing GABAergic neurons in mouse
641 barrel cortex. Nat Neurosci 15, 607–612. doi:10.1038/nn.3051
642 Gibson, J.R., Bartley, A.F., Hays, S.A., Huber, K.M., 2008. Imbalance of neocortical excitation
643 and inhibition and altered UP states reflect network hyperexcitability in the mouse model of
644 fragile X syndrome. J Neurophysiol 100, 2615–2626. doi:10.1152/jn.90752.2008
645 Golshani, P., Gonçalves, J.T., Khoshkhoo, S., Mostany, R., Smirnakis, S., Portera-Cailliau, C.,

646 2009. Internally mediated developmental desynchronization of neocortical network activity.
647 J Neurosci 29, 10890–10899. doi:10.1523/JNEUROSCI.2012-09.2009
648 Gonçalves, J.T., Anstey, J.E., Golshani, P., Portera-Cailliau, C., 2013. Circuit level defects in
649 the developing neocortex of Fragile X mice. Nat Neurosci 16, 903–909.
650 doi:10.1038/nn.3415
651 Goodman, D.F.M., Brette, R., 2009. The brian simulator. Front Neurosci 3, 192–197.
652 doi:10.3389/neuro.01.026.2009
653 Gutenkunst, R.N., Waterfall, J.J., Casey, F.P., Brown, K.S., Myers, C.R., Sethna, J.P., 2007.
654 Universally sloppy parameter sensitivities in systems biology models. PLoS Comput Biol 3,
655 1871–1878. doi:10.1371/journal.pcbi.0030189
656 Harlow, E.G., Till, S.M., Russell, T.A., Wijetunge, L.S., Kind, P., Contractor, A., 2010. Critical
657 period plasticity is disrupted in the barrel cortex of FMR1 knockout mice. Neuron 65, 385–
658 398. doi:10.1016/j.neuron.2010.01.024
659 Hays, S.A., Huber, K.M., Gibson, J.R., 2011. Altered neocortical rhythmic activity states in
660 Fmr1 KO mice are due to enhanced mGluR5 signaling and involve changes in excitatory
661 circuitry. J Neurosci 31, 14223–14234. doi:10.1523/JNEUROSCI.3157-11.2011
662 He, Q., Nomura, T., Xu, J., Contractor, A., 2014. The developmental switch in GABA polarity is
663 delayed in fragile X mice. J Neurosci 34, 446–450. doi:10.1523/JNEUROSCI.4447-13.2014
664 Kehrer, C., Maziashvili, N., Dugladze, T., Gloveli, T., 2008. Altered Excitatory-Inhibitory
665 Balance in the NMDA-Hypofunction Model of Schizophrenia. Frontiers in Molecular
666 Neuroscience 1, 6. doi:10.3389/neuro.02.006.2008
667 Kerr, J.N.D., de Kock, C.P.J., Greenberg, D.S., Bruno, R.M., Sakmann, B., Helmchen, F., 2007.
668 Spatial organization of neuronal population responses in layer 2/3 of rat barrel cortex. J
669 Neurosci 27, 13316–13328. doi:10.1523/JNEUROSCI.2210-07.2007
670 Kinnischtzke, A.K., Sewall, A.M., Berkepile, J.M., Fanselow, E.E., 2012. Postnatal maturation
671 of somatostatin-expressing inhibitory cells in the somatosensory cortex of GIN mice. Front
672 Neural Circuits 6, 33. doi:10.3389/fncir.2012.00033
673 La Fata, G., Gärtner, A., Domínguez-Iturza, N., Dresselaers, T., Dawitz, J., Poorthuis, R.B.,
674 Averna, M., Himmelreich, U., Meredith, R.M., Achsel, T., Dotti, C.G., Bagni, C., 2014.
675 FMRP regulates multipolar to bipolar transition affecting neuronal migration and cortical
676 circuitry. Nat Neurosci. doi:10.1038/nn.3870
677 Lefort, S., Tomm, C., Floyd Sarria, J.-C., Petersen, C.C.H., 2009. The excitatory neuronal
678 network of the C2 barrel column in mouse primary somatosensory cortex. Neuron 61, 301–
679 316. doi:10.1016/j.neuron.2008.12.020
680 Lu, H., Ash, R.T., He, L., Kee, S.E., Wang, W., Yu, D., Hao, S., Meng, X., Ure, K., Ito-Ishida, A.,
681 Tang, B., Sun, Y., Ji, D., Tang, J., Arenkiel, B.R., Smirnakis, S.M., Zoghbi, H.Y., 2016.
682 Loss and Gain of MeCP2 Cause Similar Hippocampal Circuit Dysfunction that Is Rescued
683 by Deep Brain Stimulation in a Rett Syndrome Mouse Model. Neuron 91, 739–747.
684 doi:10.1016/j.neuron.2016.07.018
685 Luczak, A., Bartho, P., Harris, K.D., 2009. Spontaneous events outline the realm of possible
686 sensory responses in neocortical populations. Neuron 62, 413–425.
687 doi:10.1016/j.neuron.2009.03.014
688 Mao, T., Kusefoglu, D., Hooks, B.M., Huber, D., Petreanu, L., Svoboda, K., 2011. Long-range
689 neuronal circuits underlying the interaction between sensory and motor cortex. Neuron 72,

111–123. doi:10.1016/j.neuron.2011.07.029
Meredith, R.M., Dawitz, J., Kramvis, I., 2012. Sensitive time-windows for susceptibility in neurodevelopmental disorders. Trends Neurosci 35, 335–344. doi:10.1016/j.tins.2012.03.005
Miller, J.-E.K., Ayzenshtat, I., Carrillo-Reid, L., Yuste, R., 2014. Visual stimuli recruit intrinsically generated cortical ensembles. 111, E4053–E4061. doi:10.1073/pnas.1406077111
Mitra, A., Snyder, A.Z., Blazey, T., Raichle, M.E., 2015. Lag threads organize the brain's intrinsic activity. Proc. Natl. Acad. Sci. U.S.A. 112, E2235–E2244. doi:10.1073/pnas.1503960112
O'Leary, T., Sutton, A.C., Marder, E., 2015. Computational models in the age of large datasets. Curr Opin Neurobiol 32C, 87–94. doi:10.1016/j.conb.2015.01.006
Paluszkiewicz, S.M., Olmos-Serrano, J.L., Corbin, J.G., Huntsman, M.M., 2011. Impaired inhibitory control of cortical synchronization in fragile X syndrome. J Neurophysiol 106, 2264–2272. doi:10.1152/jn.00421.2011
Patel, A.B., Hays, S.A., Bureau, I., Huber, K.M., Gibson, J.R., 2013. A target cell-specific role for presynaptic Fmr1 in regulating glutamate release onto neocortical fast-spiking inhibitory neurons. J Neurosci 33, 2593–2604. doi:10.1523/JNEUROSCI.2447-12.2013
Petersen, C.C.H., Crochet, S., 2013. Synaptic computation and sensory processing in neocortical layer 2/3. Neuron 78, 28–48. doi:10.1016/j.neuron.2013.03.020
Petreanu, L., Huber, D., Sobczyk, A., Svoboda, K., 2007. Channelrhodopsin-2-assisted circuit mapping of long-range callosal projections., Nature neuroscience. doi:10.1038/nn1891
Pologruto, T.A., Yasuda, R., Svoboda, K., 2004. Monitoring neural activity and [Ca2+] with genetically encoded Ca2+ indicators. J Neurosci 24, 9572–9579. doi:10.1523/JNEUROSCI.2854-04.2004
Qian, N., Lipkin, R.M., 2011. A learning-style theory for understanding autistic behaviors. Front Hum Neurosci 5, 77. doi:10.3389/fnhum.2011.00077
Quian Quiroga, R., Panzeri, S., 2009. Extracting information from neuronal populations: information theory and decoding approaches. Nat Rev Neurosci 10, 173–185. doi:10.1038/nrn2578
Ringach, D.L., 2009. Spontaneous and driven cortical activity: implications for computation. Curr Opin Neurobiol 19, 439–444. doi:10.1016/j.conb.2009.07.005
Rochefort, N.L., Garaschuk, O., Milos, R.-I., Narushima, M., Marandi, N., Pichler, B., Kovalchuk, Y., Konnerth, A., 2009. Sparsification of neuronal activity in the visual cortex at eye-opening. 106, 15049–15054. doi:10.1073/pnas.0907660106
Rubenstein, J.L.R., Merzenich, M.M., 2003. Model of autism: increased ratio of excitation/inhibition in key neural systems. Genes Brain Behav. 2, 255–267.
Sato, T.R., Gray, N.W., Mainen, Z.F., Svoboda, K., 2007. The functional microarchitecture of the mouse barrel cortex. PLoS Biol 5, e189. doi:10.1371/journal.pbio.0050189
Schneidman, E., Berry, M.J., Segev, R., Bialek, W., 2006. Weak pairwise correlations imply strongly correlated network states in a neural population. Nature 440, 1007–1012. doi:10.1038/nature04701
Selby, L., Zhang, C., Sun, Q.-Q., 2007. Major defects in neocortical GABAergic inhibitory circuits in mice lacking the fragile X mental retardation protein. Neurosci. Lett. 412, 227–

232. doi:10.1016/j.neulet.2006.11.062

Testa-Silva, G., Loebel, A., Giugliano, M., de Kock, C.P.J., Mansvelder, H.D., Meredith, R.M., 2012. Hyperconnectivity and slow synapses during early development of medial prefrontal cortex in a mouse model for mental retardation and autism. Cereb Cortex 22, 1333–1342. doi:10.1093/cercor/bhr224

Tomm, C., Avermann, M., Petersen, C., Gerstner, W., Vogels, T.P., 2014. Connection-type-specific biases make uniform random network models consistent with cortical recordings. J Neurophysiol 112, 1801–1814. doi:10.1152/jn.00629.2013

Wallace, M.L., Burette, A.C., Weinberg, R.J., Philpot, B.D., 2012. Maternal loss of Ube3a produces an excitatory/inhibitory imbalance through neuron type-specific synaptic defects. Neuron 74, 793–800. doi:10.1016/j.neuron.2012.03.036

Yaksi, E., Friedrich, R.W., 2006. Reconstruction of firing rate changes across neuronal populations by temporally deconvolved Ca2+ imaging. Nat. Methods 3, 377–383. doi:10.1038/nmeth874